A quantum reactive scattering perspective on electronic nonadiabaticity

Yang Peng, Luca M. Ghiringhelli, and Heiko Appel*
Fritz-Haber-Institut der Max-Planck-Gesellschaft, Faradayweg 4-6, 14195, Berlin, Germany
(Dated: May 28, 2014)

Based on quantum reactive-scattering theory, we propose a method for studying the electronic nonadiabaticity in collision processes involving electron-ion rearrangements. We investigate the state-to-state transition probability for electron-ion rearrangements with two comparable approaches. In the first approach the information of the electron is only contained in the ground-state Born-Oppenheimer potential-energy surface, which is the starting point of common reactive-scattering calculations. In the second approach, the electron is explicitly taken into account and included in the calculations at the same level as the ions. Hence, the deviation in the results between the two approaches directly reflects the electronic nonadiabaticity during the collision process. To illustrate the method, we apply it to the well-known proton-transfer model of Shin and Metiu, generalized in order to allow for reactive scattering channels. We show that our explicit electron approach is able to capture electronic nonadiabaticity and the renormalization of the reaction barrier near the classical turning points of the potential in nuclear configuration space. In contrast, system properties near the equilibrium geometry of the asymptotic scattering channels are hardly affected by electronic nonadiabatic effects. We also present an analytical expression for the transition amplitude of the asymmetric proton-transfer model based on the direct evaluation of integrals over the involved Airy functions.

I. INTRODUCTION

The fundamental understanding of elementary chemical reactions is an important subject in chemical physics. The development of molecular-beam scattering techniques has made it possible to experimentally study detailed state-to-state dynamics of gas phase reactions[1–3]. On the other hand, the interest for developing reactive-scattering theories to describe chemical reactions arose much earlier, shortly after the discovery of quantum mechanics[4, 5], when it was realized that the Born-Oppenheimer (BO) approximation leads naturally to the concept of potential-energy surfaces (PES), that govern the motion of atoms during a chemical reaction. The PES play such a crucial role as the potential governing the dynamics of the nuclei, that almost all reactive-scattering approaches, either classical[6] or quantum[7], are using PES data as initial input. For many cases, the ground-state BO PES is sufficient for the description of scattering events[8], since the motion of the nuclei is typically much slower than that of the electrons so that electrons can be assumed to be effectively in the ground state. In this respect, the notion of electronic nonadiabaticity is identified with the set of all those ingredients that are missed when assuming that the motion of atoms is governed by the lowest (ground-state) PES.

It is not uncommon to find situations where nonadiabaticity plays an important role[9–13]. Such examples encompass reactions involving light ions, charge transfer and photochemical processes[14–16]. To capture this type of nonadiabaticity, reactive-scattering treatments involving excited PESs were developed[17], which allow to take into account the electronic excitations during scattering. In general, these approaches use as *a priori* inputs, besides several ground- and excited-states PESs, the nonadiabatic coupling terms[18] between different surfaces. Such coupling terms can nowadays be directly calculated through e.g. the linear-response formalism of time-dependent density-functional theory[19–22]. However, the multi-PES scattering approach typically only involves a small number of surfaces (in most cases only the ground and first-excited PES are considered) and may not always contain all essential ingredients of electronic nonadiabaticity.

In the work presented here, instead of directly utilizing several electronic surfaces and non-adiabatic couplings as input, we choose a specific coordinate system convenient for scattering calculations which allows us to quantify electronic nonadiabaticity from a perspective that differs from the normal treatment in the literature. As an illustration of our idea, and in order to make it as clear as possible, we restrict ourselves to a simple 1D collinear model, which was originally designed to study the nonadiabatic effects in a proton-transfer reaction[23] by Shin and Metiu. We emphasize, that our approach also remains valid for ab initio Hamiltonians in full dimensionality. As many other recent studies on electronic nonadiabaticity in the literature[24–30], we solely restrict our discussion to a 1D model in order to simplify the mathematical expressions and to highlight the essence of the underlying physics.

Our paper is organized as follows. In section II, we introduce the model used for the illustration of our scattering treatments on electronic nonadiabaticity. These treatments are discussed in detail in section III, where we consider two approaches which can be compared in parallel. In the first approach, which we term implicit electron approach (cf. to section III A), we consider the electron

*E-Mail: {peng,ghiringhelli,appel}@fhi-berlin.mpg.de

implicitly, i.e. we assume that the three ions move on the ground state BO PES. In the second approach, which we call explicit electron approach (cf. to section III B), we describe the motion of all particles (three ions and one electron) simultaneously, so that the electron will be taken into account explicitly. In both sections introducing the two apporaches we tutorially derive the methods and then we summarize the algorithm. In both IE and EE approaches state-selective transition probabilities are calculated, and the results and further analyses are shown in section IV. Finally, the conclusions are given in section V.

II. MODEL

Before demonstrating our two approaches, which will be disscussed in the next section, we first present the model which we use for the illustration of our implicit and explicit electron schemes. In order to keep a clear focus on our approaches to describe electronic nonadiabaticity, we restrict ourselves here to a simple but physically motivated collinear reactive scattering model. We emphasize that it is straightforward to apply our implicit and explicit electron approaches also to ab initio Hamiltonians in full dimensionality.

Our model is quite similar to the original Shin-Metiu model, containing three ions and one electron confined to a one-dimensional collinear motion. In order to investigate reactive scattering with such a model, we need to include the scattering states describing asymptotic channels in which one ion is far away from the other part of the system. In other words, we need to remove the constraint of fixed terminal ions, to allow all ions to move along the 1D line. This generalization of the original Shin-Metiu model is sketched in figure 1. Allowing all ions to move enables us to describe the transition from the in-channel configuration to the out-channel configuration through a collinear collision. This process involves transfers of both an ion and an electron.

The Hamiltonian of our extended Shin-Metiu model can be written as

$$\hat{H} = \hat{T}_N + \hat{T}_e + V_{NN} + V_{eN}, \tag{1}$$

where $\hat{T}_N$ is the kinetic energy of the three ions

$$\hat{T}_N = -\frac{\partial_A^2}{2M_A} - \frac{\partial_B^2}{2M_B} - \frac{\partial_C^2}{2M_C}, \tag{2}$$

and the kinetic energy of the electron is $\hat{T}_e = -\partial_e^2/2m_e$ (atomic units are used throughout). Since we allow the ions A and C to move, the masses M_A and M_C are in general finite (the infinite mass limit corresponds to the original model of fixed ions). Here we focus on a case where M_A and M_C are large compared to the mass M_B in the center. This allows us to model a light-atom transfer process. We emphasize that the positions of A and C could also be viewed as center-of-mass cordinates of small clusters or nano-particles motivating further a small mass ratio $M_B/M_{A,C}$. The most important parameter for electronic nonadiabaticity in the present model is therefore the mass ratio between the middle ion and the electron. The masses of the ions at the terminal positions do not play an essential role in our discussion as long as they are much larger than the mass M_B of the ion in the center.

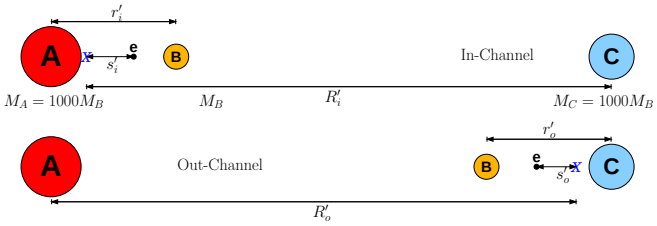

FIG. 1: Schematic representation of our generalization of the Shin-Metiu model. In contrast to the original Shin-Metiu model, we allow all ions to move in the present study. Two asymptotic channels (in and out) are considered. The in-channel describes a bound system of ions A, B, and the electron. Ion C is initially located far from this bound system. The out-channel describes a bound system of ions B, C, and the electron. Here, ion C is located far from the bound complex. Transitions from the in-channel to the out-channel involve a simultaneous electron-ion rearrangement.

In atomic units, we take $M_A = 1000M_B$, $M_C = 1000M_B$, $m_e = 1$. For the center ion we consider two cases (i) $M_B = 1836m_e \sim m_H$ and (ii) $M_B = 3\times 1836m_e \sim 3m_H$, i.e. the mass of the ion B is taken to be the proton mass or 3 times the proton mass. It is expected that the electronic nonadiabaticity differs in the two cases. The interaction between the ions is given by $V_{NN} = V_{AB} + V_{BC} + V_{CA}$, where we choose short range interactions with the following form

$$V_{AB} = \frac{h_{AB}\alpha_{AB}^2}{\sinh^2\left(\alpha_{AB}(X_A - X_B)\right)}. \tag{3}$$

Here, h_{AB} and α_{AB} are parameters that tune the strength and the range of the interaction. We employ similar expressions for V_{BC} and V_{CA}. With $V_{eN} = V_{eA} + V_{eB} + V_{eC}$ we denote the electron-ion interaction which we also choose to be short ranged and given by the following form

$$V_{eA} = -\frac{g_A\beta_A^2}{\cosh^2\left(\beta_A(x_e - X_A)\right)}. \tag{4}$$

With $X_{\{A,B,C\}}$ and x_e, we denote the ionic and electronic coordinates respectively. Again, g_A and β_A are parameters characterizing the strength and the range of the potential. Similar expressions are employed for V_{eB} and V_{eC}. Such a choice of interaction potentials qualitatively captures a realistic situation in which ions are repulsive to each other and are attractive to the electron. The short range potentials chosen here are for the convenience of the scattering calculations.

One feature of the chosen potentials that should be highlighted is that the ion-ion repulsion is singular at zero separation. This imposes the constraint that the ions cannot bypass each other, or in other words, the ions preserve the order during the scattering process. Hence, we only need to consider two asymptotic channels (cf. figure 1). On the other hand, the electron-ion attraction is soft at zero separation, which allows the electron to pass the ions. In order to illustrate our approach, we choose in the present work for the range parameters $\alpha_{AB} = \alpha_{BC} = \alpha_{CA} = 0.70$, and $\beta_A = \beta_B = \beta_C = 1.70$. The interaction strengths are given by $h_{BC} = 1.00$, $h_{AB} = h_{CA} = 1.002$, and $g_A = 1.002$, $g_B = g_C = 1.00$. The parameters are chosen to produce a physical potential-energy surface for rearrangement scattering. Note, that it is predominantely the masses and not the interaction parameters that determine the magnitude of electronic nonadiabaticity.

We emphasize that in general the choice of interaction potentials is not imposing any restrictions on our approach. The selected potentials and parameters are physically motivated, keep the present discussion simple, and allow us to focus on the central topic of this work, the description of nonadiabatic electronic motion in electron-ion rearrangement collisions.

III. QUANTUM REACTIVE SCATTERING TREATMENT

In this section, we introduce two quantum reactive scattering approaches to calculate the transition probabilities of the rearrangement collision. The electronic nonadiabaticity will be visualized through the comparison of the two approaches. In the first approach, the information of the electron is only contained in the ground-state BO PES. We therefore call it *implicit electron (IE) approach*. In the second approach, the electron and the three ions are considered all at the same level, i.e. we solve a four-body quantum reactive scattering problem. In the following we refer to this as *explicit electron (EE) approach*. In the two approaches, we calculate the transition (reaction) probability and thus obtain the reaction rate by taking an average over Boltzmann factors. The differences in the two approaches indicate the electronic nonadiabaticity.

The model described in the last section is used to demonstrate the two approaches. In the following discussion, we only focus on the figures for the case $M_B = m_H$ for illustrations. The plots are qualitatively very similar for the case of $M_B = 3m_H$.

A. Implicit Electron Approach

1. Coordinate System

In the IE approach on the collinear model, the three ions are moving on the ground-state PES determined by the electronic Hamiltonian, so three degrees of freedom are needed to describe the system. Since there is no external field, the system is translationally invariant. Hence, if we choose Jacobi coordinates, and separate off the degree of freedom describing the center-of-mass motion, then only two internal degrees of freedom are left, which can be chosen as $r'_i = X_B - X_A$ and $R'_i = X_C - (M_A X_A + M_B X_B)/(X_A + X_B)$ for the in-channel configuration or as $r'_o = X_C - X_B$ and $R'_o = (M_B X_B + M_C X_C)/(M_B + M_C)$ for the out-channel configuration. Each set of coordinates has its merits in describing a particular configuration of the system. However, in order to describe the whole scattering process using one set of coordinates, we employ in the following a mass-weighted hyperspherical coordinate system[31]. To this end, we first define mass-weighted coordinates as

$$r_i = \sqrt{\frac{\mu_{AB}}{m}} r'_i, \qquad R_i = \sqrt{\frac{\mu_{C,AB}}{m}} R'_i, \tag{5a}$$

$$r_o = \sqrt{\frac{\mu_{BC}}{m}} r'_o, \qquad R_o = \sqrt{\frac{\mu_{A,BC}}{m}} R'_o, \tag{5b}$$

in which the μ's denote different reduced masses. For example, μ_{AB} is the reduced mass of A and B, $\mu_{C,AB}$ is the reduced mass of C and the center-of-mass of AB. m is an arbitrary mass, we choose it to be equal to M_B in this paper. The two new sets of coordinates have the noteworthy property

$$r_i^2 + R_i^2 = r_o^2 + R_o^2, \tag{6}$$

which allows us to introduce a polar coordinate system by defining

$$\rho = \sqrt{r_i^2 + R_i^2} = \sqrt{r_o^2 + R_o^2} \tag{7a}$$

$$\theta = \arctan(r_i/R_i) = \theta_m - \arctan(r_o/R_o). \tag{7b}$$

In terms of these new coordinates, the in-channel and out-channel configurations can be described on equal footing. It can be shown that the angle $\theta \in [0, \theta_m]$ is bounded, with

$$\theta_m = \arctan \sqrt{\frac{M_B(M_A + M_B + M_C)}{M_A M_C}}. \tag{8}$$

2. Hamiltonian

The Hamiltonian in the above introduced mass-weighted hyperspherical coordinate system can be written as

$$\hat{H} = -\frac{1}{2m}\left[\frac{\partial^2}{\partial\rho^2} + \frac{1}{\rho}\frac{\partial}{\partial\rho} + \frac{1}{\rho^2}\frac{\partial^2}{\partial\theta^2}\right] + V(\rho, \theta), \tag{9}$$

where $V(\rho, \theta)$ is the ground-state BO surface shown in figure 2 for the case $M_B = m_H$. For every given nuclear configuration, we solve for the ground-state BO surface

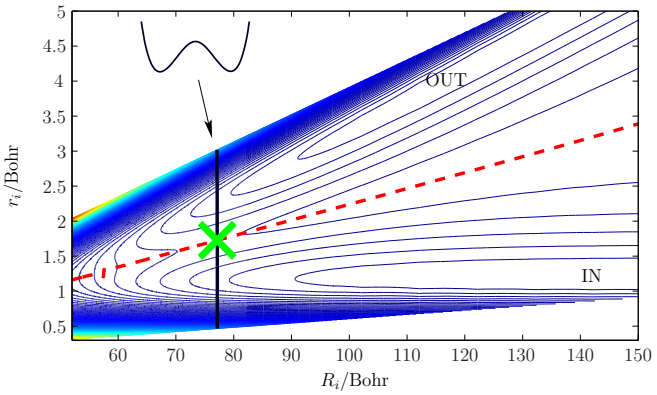

FIG. 2: Ground-state BO surface $V(\rho,\theta)$ for the model ($M_B = m_H$) in the mass-weighted hyperspherical coordinate system, with the corresponding Cartesian coordinates (r_i, R_i). Note the two very different scales of the axes. The green cross indicates the position of the classical transition state. It is the energy minimum along the red dashed line, and the maximum along the black solid cut for a constant ρ. The shape of $V(\rho,\theta)$ along the black solid cut is schematically sketched in the inset in the top-left corner. The two valleys in the plot can be identified to either describe in-channel or out-channel configurations.

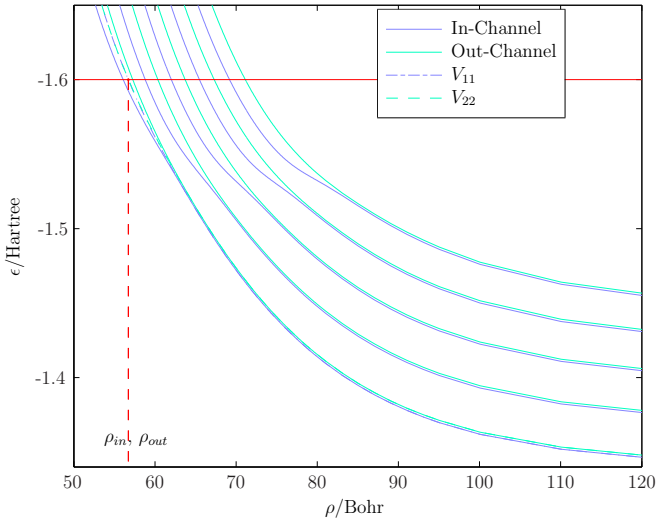

FIG. 3: The lowest ten eigenvalues $\epsilon_i(\rho)$ of the angular Hamiltonian (for the case $M_B = m_H$) as a function of the radius are shown with solid lines. The two colors denote either eigenstates with in-channel (localized in the in-channel valley) or out-channel-like (localized in the out-channel valley) character. The dashed-dotted lines V_{11} and V_{22} are the energies corresponding to maximally localized states obtained after mixing the original in-channel and out-channel-like states (see text).

by exact diagonalization of the electronic Hamiltonian in a finite-difference representation in hyperspherical coordinates.

In figure 2, it can be seen that for a given radius ρ, the cut along θ has a double-well shape, and the minimum corresponds to either the in-channel or the out-channel configuration. From the scale of the coordinate axes it is obvious that the radius ρ is a slow variable compared to the angle θ, which implies that the two variables are approximately decoupled.

We therefore perform the hyperspherical expansion for the eigenstates of the Hamiltonian by regarding the radius as a parameter[32–34]

$$\Psi_n(\rho,\theta) = \rho^{-\frac{1}{2}} \sum_n \varphi_n(\rho)\chi_n(\theta;\rho), \qquad (10)$$

where $\{\chi_n(\theta;\rho)\}$ is a set of complete orthonormal functions of θ for a given ρ. This expansion can be truncated by choosing a proper set of functions $\{\chi_n(\theta;\rho)\}$.

In order to compute the χ_n, we first solve the angular part of the Hamiltonian for a given ρ

$$\left[-\frac{1}{2m\rho^2}\frac{\partial^2}{\partial\theta^2} + V(\rho,\theta)\right]\eta_i(\theta;\rho) = \epsilon_i(\rho)\eta_i(\theta;\rho), \qquad (11)$$

where $\eta_i(\theta;\rho)$ is the eigenfunction with eigenvalue $\epsilon_i(\rho)$ for a given ρ. The eigenvalues $\epsilon_i(\rho)$ of the angular Hamiltonian are shown in figure 3. The curves are plotted in two different colors depending on whether they are in-channel states or out-channel states, according to where the wave function is localized. The relative position between the two sets of curves is very sensitive to the input parameters (masses and interaction strength), and in our case we choose the interaction parameters to be asymmetric to avoid degeneracies in these curves. This allows to unambiguously identify the nondegenerate asymptotic states as vibrational states of in- or out-channel configurations. For our setup, it can be seen that these eigenvalues appear in pairs. The wave functions in a given pair also specify the internal vibrational states of the initial and final scattering wave functions. The scattering from a given in-channel configuration to a given out-channel configuration can be related to a transtion within a pair. Since the two wave functions in a pair span a 2-dimensional space that is approximately decoupled from the space spanned by the wave functions belonging to other pairs (inter-pair distances are large), by considering each pair separately, we can have a state-to-state description of the reaction, which is the advantage of reactive-scattering theory. To make the illustration as simple as possible, in the following we only take the lowest pair, within which the transition gives the main contribution to the transition probability since this pair is energetically more favourable.

The angular potential $V(\theta;\rho)$ along a fixed ρ cut is shown in figure 4. The wave functions belonging to the lowest pair are also given in this figure. The one localized in the left valley (η_1) is an in-channel state, and corresponds to the ground-vibrational state of the AB molecule (zero nodes). The other one (η_2), localized in the right valley, is an out-channel state, and can be interpreted as the ground-vibrational state of the BC

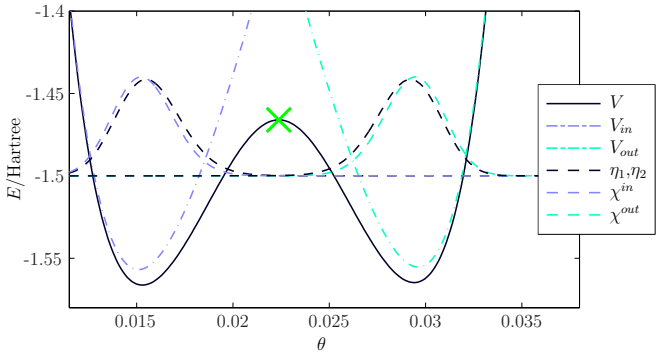

FIG. 4: Angular potential $V(\rho,\theta)$ for the case $M_B = m_H$ (black solid line) along the cut across the saddle point on the PES. The angular wave functions of the lowest pair η_1 and η_2, both in black dashed lines, are localized in one of the two minima of the double well, corresponding to an in-channel (left) or an out-channel (right) state. The maximally localized states χ^{in} and χ^{out} obtained by mixing η_1 and η_2 are plotted in dashed lines in different colors. The V_{in} and V_{out} for the localization scheme are plotted with dashed-dotted lines in the same color setting for χ^{in} and χ^{out}.

molecule (zero nodes). If we choose χ_1 and χ_2 that span the same space spanned by η_1 and η_2, then the expansion in Eq. (10) can be approximately written as a linear combination of χ_1 and χ_2. Moreover, if χ_1 and χ_2 are chosen to be maximally localized wave functions in one of the valleys, then the full asymptotic wave function for in-channel and out-channel configurations can be written as

$$\Psi^{in}_{\nu=0}(\rho,\theta) = \rho^{-1/2}\varphi_1(\rho)\chi_1(\theta;\rho) \tag{12}$$
$$\Psi^{out}_{\nu=0}(\rho,\theta) = \rho^{-1/2}\varphi_2(\rho)\chi_2(\theta;\rho). \tag{13}$$

To get the maximally localized wave functions, which best represent the two asymptotic channels, we first define two auxilliary potentials V_{in} and V_{out}

$$V_{in}(\rho,\theta) = V(\rho,\theta) - V_{eC}(\rho,\theta) \tag{14a}$$
$$V_{out}(\rho,\theta) = V(\rho,\theta) - V_{eA}(\rho,\theta). \tag{14b}$$

The potentials V_{eC} and V_{eA} describe the attraction from ion C and A respectively. The two auxiliary potentials, that have only one valley, are also shown in figure 4. We mix the wave functions η_1 and η_2 by defining an orthogonal transformation

$$\begin{pmatrix}\chi_1\\ \chi_2\end{pmatrix} = \mathbf{T}\begin{pmatrix}\eta_1\\ \eta_2\end{pmatrix} = \begin{pmatrix}\cos\zeta & -\sin\zeta\\ \sin\zeta & \cos\zeta\end{pmatrix}\begin{pmatrix}\eta_1\\ \eta_2\end{pmatrix}, \tag{15}$$

where $\zeta \in [0, \frac{\pi}{2}]$. The parameter ζ is chosen such that the quantity

$$I = \left|\left\langle \chi^{in} \,|\, \chi_1 \right\rangle\right|^2 + \left|\left\langle \chi^{out} \,|\, \chi_2 \right\rangle\right|^2 \tag{16}$$

is maximized. The χ^{in} and χ^{out} are eigenfunctions of the auxiliary potentials, with the same number of nodes as the original wave functions η_1 and η_2. The physical meaning is that we want to mix η_1 and η_2 such that the new wave functions maximally overlap with the exact localized functions.

To obtain the transformation matrix $\mathbf{T}$, we regard ζ as a variational parameter. Optimizing the localization as function of ζ yields

$$I(\zeta)' = B\sin 2\zeta + 2A\cos 2\zeta, \tag{17}$$

where

$$A = \left\langle \chi^{out} \,|\, \eta_1 \right\rangle\left\langle \chi^{out} \,|\, \eta_2 \right\rangle - \left\langle \chi^{in} \,|\, \eta_1 \right\rangle\left\langle \chi^{in} \,|\, \eta_2 \right\rangle, \tag{18a}$$
$$B = \left\langle \chi^{in} \,|\, \eta_2 \right\rangle^2 + \left\langle \chi^{out} \,|\, \eta_1 \right\rangle^2 - \left\langle \chi^{in} \,|\, \eta_1 \right\rangle^2 - \left\langle \chi^{out} \,|\, \eta_2 \right\rangle^2. \tag{18b}$$

By setting $I(\zeta_0)' = 0$, we get $\tan 2\zeta_0 = -2A/B$. To maximize this quantity, we have $I(\zeta_0)'' \le 0$, which yields $A\sin 2\zeta \ge 0$. Since there is arbitrariness in choosing the relative phase of the state $|\,\eta_1\,\rangle$, $|\,\eta_2\,\rangle$, $|\,\chi^{in}\,\rangle$ and $|\,\chi^{out}\,\rangle$, we fix it by choosing the phase such that $\left\langle \chi^{in} \,|\, \chi^{out} \right\rangle \le 0$ and $A \le 0$. Hence, we arrive at

$$\sin 2\zeta = \frac{2A}{\sqrt{4A^2+B^2}}, \tag{19a}$$
$$\cos 2\zeta = \frac{B}{\sqrt{4A^2+B^2}}, \tag{19b}$$

for the optimal parameter ζ.

3. *Distorted Wave Born Approximation (DWBA)*

We follow the approach described in Ref. [32–34] for calculating the transiton probability. The transition within the lowest pair, i.e. $\nu_{AB} = 0 \to \nu_{BC} = 0$, is determined by the coupled equations

$$\left[-\frac{1}{2m}\frac{\partial}{\partial\rho^2} - \frac{1}{8m\rho^2} + V_{11}(\rho) - E\right]\varphi_1(\rho) = -V_{12}(\rho)\varphi_2(\rho), \tag{20a}$$
$$\left[-\frac{1}{2m}\frac{\partial}{\partial\rho^2} - \frac{1}{8m\rho^2} + V_{22}(\rho) - E\right]\varphi_2(\rho) = -V_{21}(\rho)\varphi_1(\rho), \tag{20b}$$

where

$$V_{ij}(\rho) = \int d\theta\chi_i(\theta,\rho)\left[-\frac{1}{2m\rho^2}\frac{\partial^2}{\partial\theta^2} + V(\rho,\theta)\right]\chi_j(\rho,\theta). \tag{21}$$

By using Eq. (19), it can be shown that

$$V_{12}(\rho) = V_{21}(\rho) = \frac{A}{\sqrt{4A^2+B^2}}(\epsilon_1-\epsilon_2) > 0, \tag{22a}$$
$$V_{11}(\rho) = \frac{\epsilon_1+\epsilon_2}{2} + \frac{B(\epsilon_1-\epsilon_2)}{2\sqrt{4A^2+B^2}}, \tag{22b}$$
$$V_{22}(\rho) = \frac{\epsilon_1+\epsilon_2}{2} - \frac{B(\epsilon_1-\epsilon_2)}{2\sqrt{4A^2+B^2}}, \tag{22c}$$

where ϵ_1 and ϵ_2 are the angular eigenvalues in the lowest pair ($\epsilon_1 < \epsilon_2$) parametrically depending on the radius ρ. The two diagonal terms V_{11} and V_{22} are plotted in figure 3.

To arrive at the transition probability, the coupled differential equations could be solved e.g. numerically. However, as we will demonstrate in the following, using the DWBA allows us to arrive at an *analytical* expression for the transition amplitude. Low-energy scattering events which are the prototypical case for many chemical applications are covered well in this approximation as known from previous studies[32–34]. Our analytical result for the amplitude provides therefore a useful and efficient tool for the analysis of nonadiabatic effects and the comparision of our IE and EE approaches.

The transition amplitude in DWBA can be written as

$$t_{21} = m \int_0^\infty d\rho \varphi_2^0(\rho) V_{12}(\rho) \varphi_1^0(\rho) \tag{23}$$

in which the wave functions φ_1^0 and φ_2^0 are solutions of Eq. (20) by setting the right-hand sides to zero. The transition probability can be written as

$$P_{21} = \sin^2(2\pi t_{21}), \tag{24}$$

known as the exponential DWBA[35].

To allow for an analytical evaluation of t_{12}, some approximations have to be taken. First, we linearize the potential near the classical turning points ρ_{in} and ρ_{out} (see figure 3), since the major part of the contribution to the integral comes from a narrow range near that point

$$\left(E - V_{11}(\rho) + \frac{1}{8m\rho^2}\right) = (\rho - \rho_{in})\, F_{in} \tag{25a}$$

$$\left(E - V_{22}(\rho) + \frac{1}{8m\rho^2}\right) = (\rho - \rho_{out})\, F_{out}. \tag{25b}$$

The term $1/8m\rho^2$ is much smaller than V_{11}, so the turning points ρ_{in} and ρ_{out} are almost the values of ρ at the cross point between the horizontal red line of a given energy and the $V_{ii}(\rho)$ of the maximally localized states, as shown in figure 3. F_{in} and F_{out} are the corresponding first-order derivatives with respect to ρ at the turning point. We can directly write down the unperturbed wave function, which are given in terms of Airy functions, Ai($\cdot$)

$$\varphi_1^0(\rho) = (2/B_{in})^{1/2} \mathrm{Ai}(-B_{in}(\rho - \rho_{in})), \tag{26a}$$

$$\varphi_2^0(\rho) = (2/B_{out})^{1/2} \mathrm{Ai}(-B_{out}(\rho - \rho_{out})), \tag{26b}$$

with $B_j = (2mF_j)^{1/3}$. We define the averaged turning point

$$\rho_0 = \frac{\rho_{in} + \rho_{out}}{2} \tag{27}$$

and approximate the coupling V_{12} near this point, as in Ref. [32–34], by

$$V_{12}(\rho) = V_{12}^0 e^{-c(\rho - \rho_0)} \tag{28}$$

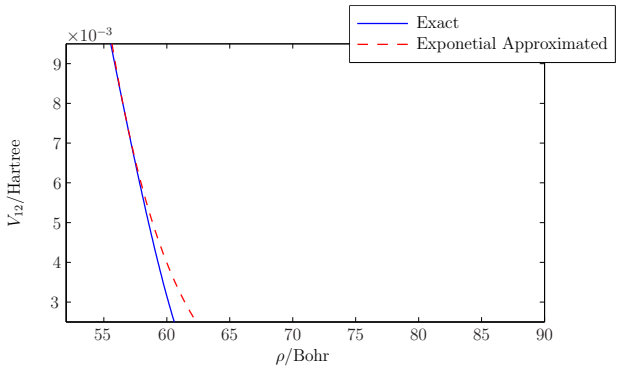

FIG. 5: The blue-solid line illustrates the coupling term (for the case $M_B = m_H$) obtained by Eq. (22a). The red-dashed line shows the exponential approximation for the coupling near the averaged turning point ρ_0.

as shown in figure 5.

Hence, the transition amplitude can be written as

$$t_{21} \simeq \frac{2mV_{12}^0}{\sqrt{B_{in}B_{out}}} \int_{-\infty}^{\infty} dx \mathrm{Ai}(-B_{in}(x-s)) \mathrm{Ai}(-B_{out}x) e^{-cx} \tag{29}$$

where $s = \rho_{in} - \rho_{out}$. We can approximately extend the lower limit of the integral to $-\infty$ due to the exponential decay of the two Airy functions. The integral can be evaluated analytically, obtaining

$$t_{21} = \frac{2mV_{12}^0}{\sqrt{B_{in}B_{out}}} \frac{e^{\sigma} \mathrm{Ai}(\xi)}{|B_{in}^3 - B_{out}^3|^{1/3}}, \tag{30a}$$

where σ and ξ are given by

$$\sigma = \frac{c^3(B_{in}^3 + B_{out}^3)}{3(B_{in}^3 - B_{out}^3)^2} - \frac{csB_{in}^3}{B_{in}^3 - B_{out}^3} \tag{30b}$$

$$\xi = \frac{c^2 B_{in} B_{out}}{(B_{in}^3 - B_{out}^3)^{4/3}} - \frac{sB_{in}B_{out}}{(B_{in}^3 - B_{out}^3)^{1/3}}. \tag{30c}$$

The derivation of this expression is shown in detail in the appendix. Equation 30a is one of the central results in the present work. It allows us to express state-to-state resolved transition probabilities directly in terms of a linearized solution around the averaged classical turning point ρ_0. In the appendix we also demonstrate that in the limit of a symmetric model our result in Eq. 30a reduces to the well known expression of Marcus and coworkers for proton transfer[32].

In summary, in practical calculations the IE scheme amounts to the following steps:

- Calculate the ground-state PES $V(\rho, \theta)$ and the auxilliary potentials $V_{in}(\rho, \theta)$ and $V_{out}(\rho, \theta)$ in the hyperspherical coordinates, which can be obtained from any ab-initio method. This is the most time consuming step.
- For each radius ρ, solve the angular eigenvalue equation (11) with $V(\rho, \theta)$, and choose the pairs that are of interest for state-selective rates.

- Solve the auxilliary angular eigenvalue equation with $V_{in}(\rho,\theta)$ and $V_{out}(\rho,\theta)$, and use the corresponding states to compute V_{11}, V_{22} and V_{12} according to equation (22).
- Use equations (24) and (30) to calculate the transition amplitude and probability.

B. Explicit Electron Approach

So far we have discussed an implicit electron approach, where the contribution of the electron is only taken into account through the BO potential energy surface. In this section we consider an explicit electron (EE) approach which does not rely on ground-state BO surfaces and treats the electron on equal footing with the nuclei during the scattering process.

1. Coordinate System

In the EE approach, after separating off the center-of-mass motion, we have three degrees of freedom describing the relative motion of the system containing three ions and one electron. Similar to the IE approach, the mass-weighted hyperspherical coordinate system is chosen. In particular, we first define the mass-weighted Jacobi coordinates for the in-channel

$$r_i = \sqrt{\frac{\mu_{AB}}{m}}\,(X_B - X_A) \tag{31a}$$

$$s_i = \sqrt{\frac{\mu_{e,AB}}{m}}\left(x_e - \frac{M_A X_A + M_B X_B}{M_A + M_B}\right) \tag{31b}$$

$$R_i = \sqrt{\frac{\mu_{C,ABe}}{m}}\left(X_C - \frac{M_A X_A + M_B X_B + m_e x_e}{M_A + M_B + m_e}\right) \tag{31c}$$

and for the out-channel

$$r_o = \sqrt{\frac{\mu_{BC}}{m}}\,(X_C - X_B) \tag{32a}$$

$$s_o = \sqrt{\frac{\mu_{e,BC}}{m}}\left(\frac{M_B X_B + M_C X_C}{M_B + M_C} - x_e\right) \tag{32b}$$

$$R_o = \sqrt{\frac{\mu_{A,BCe}}{m}}\left(\frac{M_B X_B + M_C X_C + m_e x_e}{M_B + M_C + m_e} - X_A\right). \tag{32c}$$

Since the electron is much lighter than the three ions, both, the r and R defined here are almost equal to the ones defined in the IE approach.

Similar to the IE approach, the two sets of coordinates are related through

$$r_i^2 + R_i^2 + s_i^2 = r_o^2 + R_o^2 + s_o^2. \tag{33}$$

Hence, we define the radius as

$$\rho = \sqrt{r_i^2 + R_i^2 + s_i^2}. \tag{34}$$

In addition we define two angular arguments. One is similar to the previous approach,

$$\theta = \arctan(r_i/R_i) = \theta_m - \arctan(r_o/R_o) \tag{35a}$$

$$\theta_m = \arctan\sqrt{\frac{m_2(M_1+m_2+M_3+1)(m_2+M_3+1)}{M_1 M_3 (m_2+M_3)}}. \tag{35b}$$

The upper bound θ_m is almost the same as the one defined in the context of the IE approach. The other angular argument

$$\phi = \arccos(s_i/\rho), \qquad \phi \in [0,\pi] \tag{36}$$

is new here, and to a large extent behaving like the coordinate of the electron. In the following, we will see that the many-particle wave function along the ϕ direction is localized near $\phi = \pi/2$, which corresponds physically to the situation that the electron is always localized between AB or BC. We emphasize at this point that the choice of the hyperspherical coordinate system is not restricted to the 1D case. Similar to other studies in the literature[36] it is straightforward to extend the present discussion to the 3D case. However, the expressions become then much more involved and the presentation is less transparent. To demonstrate our approach in a clear way we therefore stay in a 1D setting.

2. Hamiltonian

The Hamiltonian in the hyperspherical coordinate system is written as

$$\hat{H} = -\frac{1}{2m}\frac{\partial}{\partial\rho^2} + \frac{\hat{L}^2}{2m\rho^2} + V(\rho,\theta,\phi), \tag{37}$$

where $\hat{L}$ is the 3D angular momentum operator, and V includes the potential energy of electron-ion attraction and ion-ion repulsion. If we extend the concept of the PES, then V is just a surface in ρ, θ and ϕ, in which ρ and θ are almost the same as the ones in the IE approach and can be regarded as the ion-like coordinates, while ϕ is the electron-like coordinate. It is this "PES" that determines the internal motion of the four-particle system and leads to the reactive scattering event.

Like in the IE approach, in this case the radius ρ can be regarded as a slow variable compared to the two angular arguments. Hence we can use the same ansatz as we did in the IE approach, i.e. we solve the angular Schrödinger equation for every given ρ

$$\left[\frac{\hat{L}^2}{2m\rho^2} + V(\rho,\theta,\phi)\right]\eta_i(\theta,\phi;\rho) = \epsilon_i(\rho)\eta_i(\theta,\phi;\rho). \tag{38}$$

Also in this case the eigenvalues appear in pairs. Similar as in the IE approach, we take only the lowest pair.

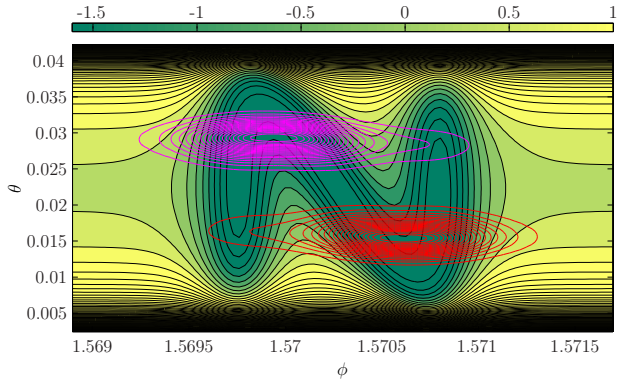

FIG. 6: Contour plot of the generalized four-body PES $V(\rho, \theta, \phi)$ (for the case $M_B = m_H$) as a function of θ and ϕ at the same ρ as in figure 4. The dark region corresponds to the valley in the surface. The lines in magenta and red are contours of the wave functions η_1, η_2 respectively, which correspond to the lowest pair in angular eigenvalues.

In figure 6, we show the generalized PES $V(\rho, \theta, \phi)$ as a function of the two angular arguments at the same radius as in figure 4. In addition we show the wave functions from the lowest pair. Instead of the double-well potential appearing in 4, here $V(\rho, \theta, \phi)$ contains a long narrow valley with zigzag structure. However, the 2D angular wave functions from the lowest pair share the same properties as the 1D wave functions in the IE approach. In particular, along θ direction, the in-channel state is localized at a smaller θ region with zero nodes, while the out-channel state is localized with zero nodes in the region with a larger θ. Along the other coordinate, the wave functions are sharply localized near the region $\phi = \pi/2$. From a geometric perspective, the wave functions are strongly confined to the equatorial plane of the sphere described by (ρ, θ, ϕ). The IE approach is obtained effectively by neglecting the smearing of the wave function out of the equatorial plane. Since ϕ to a large extent is like an electronic coordinate, we can regard this spread of the wave function as the origin of electronic nonadiabaticity. In figure 6, it can be seen that along ϕ, both wave functions have zero nodes. This is just because the electron is in the ground state in both channels.

In the following, we can apply the same localization scheme to the wave functions η_1, η_2 as we did in the IE approach in order to obtain the maximally localized states χ_1, χ_2 and the coupling term V_{12}. Then, as before, the transition probability can be calculated using the DWBA.

3. *Distorted Wave Born Approximation (DWBA)*

In this section, we calculate the transition probability within the lowest pair, which is determined by the coupled equations

$$\left[-\frac{1}{2m}\frac{\partial}{\partial\rho^2} + V_{11}(\rho) - E\right]\varphi_1(\rho) = -V_{12}(\rho)\varphi_2(\rho) \quad (39a)$$

$$\left[-\frac{1}{2m}\frac{\partial}{\partial\rho^2} + V_{22}(\rho) - E\right]\varphi_2(\rho) = -V_{21}(\rho)\varphi_1(\rho), \quad (39b)$$

where $V_{ij}(\rho)$ is given by Eq. (22), since we have taken exactly the same localization scheme as we did in the IE approach.

To calculate the transition amplitude t_{21} analytically, the same approximations for V_{ij} are taken. Thus, without any difficulties, we obtain the transition probability P_{21} by using Eq. (24).

Compared to the IE approach, for the EE approach we need to perform the following steps in practice:

- Calculate the generalized PES $V(\rho, \theta, \phi)$, the auxilliary potentials $V_{in}(\rho, \theta, \phi)$ and $V_{out}(\rho, \theta, \phi)$ for all particles (ions and the electron) at different configurations in the hyperspherical coordinates. This is the most time consuming step.
- For different radii ρ, solve the angular eigenvalue equation with the generalized PES V. Then choose the pairs that are of physical interest.
- Solve the auxilliary angular eigenvalue equation with V_{in} and V_{out}, and use the corresponding states to compute V_{11}, V_{22} and V_{12} according to equation (22). This is the same as in the IE approach.
- Use the same formulae, i.e. Eq. (30) and (24) to calculate the transition amplitude and probability.

IV. RESULTS

To visualize the electronic nonadiabaticity in the reactive scattering context, we compare the different probabilities obtained from the IE and EE approaches described above, for the two cases $M_B = m_H$ and $M_B = 3m_H$, which are shown in figure 7. The horizontal axis is the total energy of the system, which can be tuned by changing the incident kinetic energy of ion C. Since we treat the IE and EE approaches completely in parallel, the main difference between the schemes arises from whether the electron is treated explicitly or not. There are small deviations from the exact case due to the truncation in the hyperspherical expansion and the two-state approximation. However, these approximations become exact as the mass ratio between the ions in the middle and at the ends approaches zero. For the mass ratios $M_B/M_{A,C}$ considered here, which are at the order of 10^{-3}, the approximations are very accurate. Thus the deviation in the transition probability between the two approaches can almost exclusively be attributed to the difference between IE and EE, which is the main contribution of the electronic nonadiabaticity.

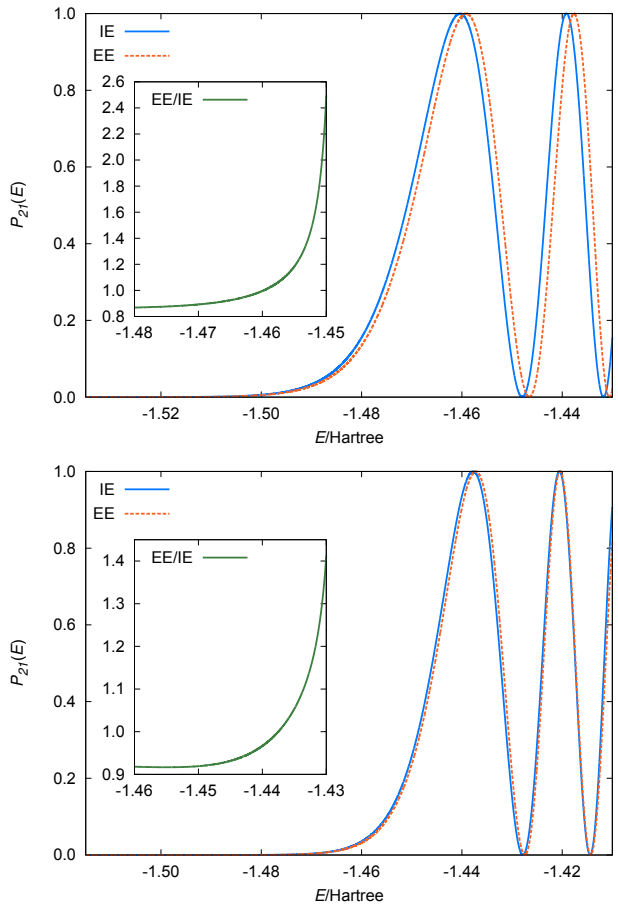

FIG. 7: Transition probability $\nu_{AB} = 0 \rightarrow \nu_{BC} = 0$ as a function of the energy of the incident ion C as obtained from the approaches of IE (blue) and EE (red). The inset in each panel is the ratio of the probabilities, obtained from the approaches of EE and IE. The upper panel shows the case $M_B = m_H$, and the lower panel displays $M_B = 3m_H$.

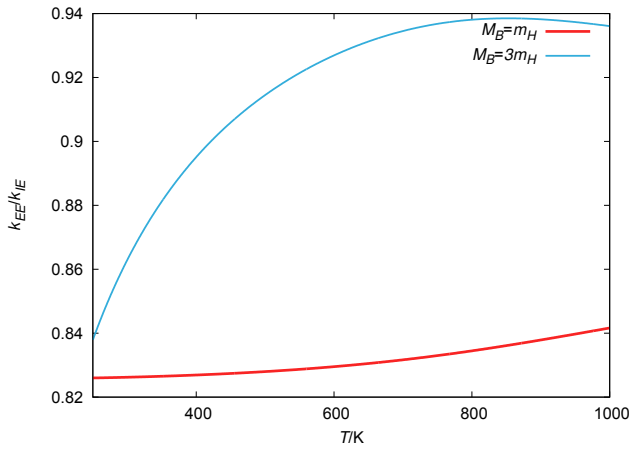

FIG. 8: The ratio k_{EE}/k_{IE} of the reaction rates for $M_B = m_H$ and $M_B = 3m_H$ from the EE and IE approaches as a function of temperature T.

In figure 7, the probability is plotted in a relatively low-energy regime, because the linear and exponential approximation for $V_{ij}(\rho)$ is only valid for low-energy scattering calculations[32–34]. From the figure, it is obvious that the rearrangement happens when the energy is above some threshold. In other words, only when the ion C has enough kinetic energy, the collision leads to a reactive rearrangement.

In low energy scattering regime, which is of chemical interests, it is shown that as the energy increases, the difference between the results from the two approaches becomes larger and larger. This directly shows the electronic nonadiabaticity is pronounced when the kinetic energy of the ions is relatively large. By comparing the results for $M_B = m_H$ and $M_B = 3m_H$, we see that the electronic nonadiabaticity is more pronounced when the mass of the central ion, or the mass ratio between the central ion and the electron, is smaller. This directly reflects the fact that the nonadiabaticity comes from the coupled motion of the electron and central ion during the rearrangement. The larger the mass ratio is, the better the traditional BO description, or similarly, the IE approach will be, as expected.

We also notice that the probability obtained in the IE approach increases faster from zero than the one in the EE approach. This implies that the rate of the rearrangement is slower in the EE approach. To see this, we calculate the ratio of the reaction rates from the two approaches for a certain range of temperatures, which is shown in figure 8. We have taken the standard expression[37] that assumes the rate is the canonical average of many collisions where the kinetic energy of the incident particle C is taken from a canonical distribution at temperature T:

$$k(T) \simeq \frac{1}{2\pi Z_{in}} \int_0^{+\infty} P_{21}(E + E_0) \exp(-\beta E) dE, \quad (40)$$

where Z_{in} is the vibrational partition function of the in-channel configuration and E_0 denotes the ground-state energy of the in-channel wavefunction. Here we approximate the contribution from transitions between all pairs by only the lowest pair. This is valid because from figure 3, the gap between the lowest pair and the pair from the 1st excited states in the asymptotic region is approximately 0.3 Hartree, which means in thermodynamic equilibrium, the population ratio between the the second lowest pair and the lowest pair according is about $\exp(-100)$, which is negligible. An alternative assumption is that the kinetic energy of the incident particle C is sharply peaked at a particular value of energy. The ratio of the reaction rates corresponds to the ratio of the two $P_{21}(E)$ curves. This ratio is shown in the insets of both panels of Fig. 7 for values of E where $P_{21}(E)$ is non negligible.

The behaviour of the ratio of the reaction rates can be understood thinking that the EE approach goes beyond the usual ground-state BO approximation and effectively considers the electronic excited states. Since

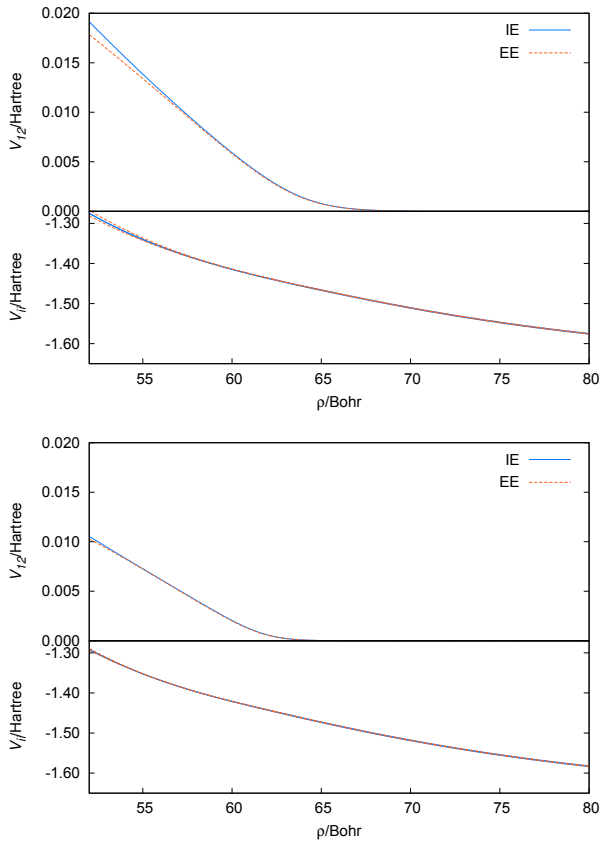

FIG. 9: The potentials $V_{12}(\rho)$, $V_{11}(\rho)$, and $V_{22}(\rho)$ as a function of radius ρ obtained from the approaches of IE (blue solid) and EE (red dashed). The upper panel displays the case for $M_B = m_H$, and the lower one for $M_B = 3m_H$.

the first excited-state surface often has a positive curvature near the maximum of the ground-state surface, as in this model[23], this implies that the excited state is energetically repulsive along the direction leading to the rearrangement. This means that any wavepacket with population restricted to the first excited state will always be bounced back, leading to nonreactive scattering. The result in the IE approach, or ground-state BO approximation, overestimates the rate which coincides with the results in the original paper of the Shin-Metiu model, which relies on a quite different approach[23]. Further, from comparing the results for the two cases with different M_B, again we see that the difference in the rate becomes larger when the central ion is lighter.

In both the IE and EE approaches, the potentials $V_{11}(\rho), V_{22}(\rho)$, and $V_{12}(\rho)$ are used as input for the DWBA calculation, which are crucial in determining the transition probability. Hence, in order explore the region at which the electronic nonadiabaticity is important, we compare the potentials obtained from the two approaches in figure 9 for the two cases with different M_B. From these figures, we notice that at large ρ, which is the situation when one ion is far apart from the other two ions and the electron, the curves from the two approaches are on top of each other. Whereas in the region of smaller ρ, the three ions get together relatively closely, or in other words near the classical transition state, there are differences between the two. For the $M_B = m_H$ case, the difference is more pronounced. This shows the electronic nonadiabaticity is most important near the barrier region or the transition state of a chemical reaction, while it hardly contributes to the property of the system in the equilibrium geometry, i.e. in the two asymptotic channels. It also shows the nonadiabaticity depends on the mass ratio of the central ion and the electron significantly. Hence, this confirms that our EE approach allows to capture electronic nonadiabaticity and the resulting renormalization of reaction barriers.

V. CONCLUDING REMARKS

In this work we proposed a scheme to capture electronic nonadiabaticity from a reactive scattering perspective. For reactive rearrangement collisions, we introduced two approaches, one which treats the electron implicitly, and a nonadiabatic approach where the electron is treated explicitly and on a similar footing as the involved ions. Both approaches rely on a mass-weighted hyperspherical coordinate system which allows for an efficient and unified representation of in- and out-channels. In particular, for the explicit electron approach the transformation to the hyperspherical coordinate system introduces a mixing of the original Cartesian coordinates of the ions and the electron, which allows to introduce approximations with smaller error compared to the original Cartesian coordinate system. Both approaches differ only in the way the electron is treated. We can therefore conclude that the differences in reaction rates obtained from both methods directly reflect the electronic nonadiabaticity.

To exemplify our approach, the original Shin-Metiu model was generalized by removing the constraint of fixed terminal ions. Within this model, we have investigated two cases, in which the mass of the central ion were set to the proton mass and three times the proton mass, while all the other system parameters were kept identical. It was shown that the electronic nonadiabaticity is larger when the mass ratio between the central ion and the electron becomes smaller. In the frame of the hyperspherical coordinate system, we found that nonadiabatic effects are much more pronounced at a small radius ρ. Physically this corresponds to regions near the reaction barrier or transition state. In contrast, nonadiabatic effects play no essential role near the equilibrium configuration in the asymptotic channels. This illustrates that our proposed approaches provide an accurate description for low-energy scattering events, which is the typical case for chemical applications. In our investigation, we showed that the electronic nonadibaticity leads to a larger deviation in transition probabilities as the energy of the system

is increasing. We also showed that the implicit electron approach overestimates the reaction rate at room temperature, since the transition probability increases faster from zero compared to the transition probabilities from the explicit electron approach. This observation is in accord with the results in earlier work[23].

The case of extremely high kinetic impact energies, which is of less interest for common chemical reactions, has not been discussed in the present work. However, we note that the nonadiabaticity in this case can be expected to play a minor role, since the scattering is fully kinetic. Collisions in this limit are fully elastic and thus do not depend at all on the intrinsic electronic structure.

The present study differs from other studies on nonadiabaticity in that the electronic nonadiabaticity was studied from a reactive-scattering perspective, and the way we treat the ions and the electron at the same footing is conceptually different from other nonadiabatic treatments based on multi-PESs. Since the quantum reactive-scattering approach describes reactions at a state-to-state resolution (in this paper we consider $\nu_{AB} = 0 \rightarrow \nu_{BC} = 0$), our approach allows to gain some insights and understanding of electronic nonadiabatic effects at a more microscopic state-to-state level.

Our way of studying the electronic nonadiabaticity can be utilized to investigate real chemical systems involving a light ion which transfers in concert with one electron in a collinear arrangement, since the approach does not depend on the mathematical form of the interactions. Future prospects include the generalization to multi-electron transfers which appear in negative-U systems, where electron transfers occur pairwise, or an extension of the present work to more sophisticated proton-coupled electron transfer reactions as studied in Refs. [38–40]. Also an embedding of the present scheme into density-functional approaches is desirable. Here further studies are required to analyze how such effective (multi-component) density-functional potentials have to be constructed.

All these aspects will be in the focus of future studies.

Acknowledgments

This research was supported by the international Max Planck research school for complex surfaces in material science (IMPRS-CS). The authors thank Professor Matthias Scheffler for his support and useful discussions and Professor John Tully for useful discussions during the preparation of the manuscript.

Appendix: Derivation of Eq. (30)

To calculate the transition amplitude, we need to evaluate an integral of the following form:

$$\begin{aligned} I &= \int_{-\infty}^{+\infty} dx \mathrm{Ai}(-b_1(x-c_1))\mathrm{Ai}(-b_2(x-c_2))e^{-ax} \\ &= \left(\frac{1}{2\pi}\right)^2 \int_{-\infty}^{+\infty} dxdydz \exp\left[if(x,y,z)\right] \end{aligned} \tag{A.1}$$

in which

$$f(x,y,z) = \frac{1}{3}(y^3+z^3)+b_1c_1y+b_2c_2z-(b_1y+b_2z)x+iax. \tag{A.2}$$

By introducing new variables

$$u = y + z \tag{A.3a}$$

$$v = b_1y + b_2z, \tag{A.3b}$$

the original variables y and z can be written in terms of the new variables

$$y = \frac{v - b_2u}{b_1 - b_2} \tag{A.4a}$$

$$z = \frac{b_1u - v}{b_1 - b_2}. \tag{A.4b}$$

Thus, we have

$$\begin{aligned} \frac{1}{3}(y^3+z^3) &= \frac{u^3}{3} - u\frac{(b_1+b_2)uv - v^2 - b_1b_2u^2}{(b_1-b_2)^2} \\ &= \frac{b_1^2+b_2^2+b_1b_2}{3(b_1-b_2)^2}u^3 + \frac{u}{(b_1-b_2)^2}\left[v^2-(b_1+b_2)uv\right] \end{aligned} \tag{A.5}$$

$$b_1c_1y + b_2c_2z = \frac{(b_1c_1-b_2c_2)}{b_1-b_2}v - \frac{b_1b_2(c_1-c_2)}{b_1-b_2}u \tag{A.6}$$

and the Jacobian takes the form

$$\left|\frac{\partial(u,v)}{\partial(y,z)}\right| = \left|\det\begin{pmatrix} 1 & 1 \\ b_1 & b_2 \end{pmatrix}\right| = |b_2 - b_1|\,. \tag{A.7}$$

Hence, The original integral can be expressed as

$$I = \left(\frac{1}{2\pi}\right)^2 \int_{-\infty}^{+\infty} \frac{dxdudv}{|b_1-b_2|} \exp(ig(x,u,v)) \tag{A.8}$$

with

$$g(x,u,v) = \frac{b_1^2+b_2^2+b_1b_2}{3(b_1-b_2)^2}u^3 - \frac{b_1b_2(c_1-c_2)}{b_1-b_2}u + iax + cu(b_1-b_2)^2\left[v^2 - \left((b_1+b_2)u + \frac{((b_1-b_2)x-(b_1c_1-b_2c_2))(b_1-b_2)}{u}\right)v\right] \quad (A.9)$$

Let

$$t = ((b_1-b_2)x-(b_1c_1-b_2c_2))(b_1-b_2), \quad (A.10)$$

then

$$x = \frac{t}{(b_1-b_2)^2} + \frac{b_1c_1-b_2c_2}{b_1-b_2} \quad (A.11a)$$

$$dx = \frac{dt}{(b_1-b_2)^2}. \quad (A.11b)$$

By applying the Gaussian integration formula

$$\int_{-\infty}^{+\infty} dv \exp(i\alpha(v^2-\beta v)) = \sqrt{\frac{i\pi}{\alpha}}\exp\left(-\frac{i\alpha\beta^2}{4}\right) \quad (A.12)$$

to Eq. (A.8), we first integrate over v and find

$$I = \left(\frac{1}{2\pi}\right)^2 \int_{-\infty}^{+\infty} \frac{dtdu}{|b_1-b_2|^3}\sqrt{\frac{i\pi}{\alpha}}\exp(ih(t,u)) \quad (A.13)$$

with

$$\alpha = \frac{u}{(b_1-b_2)^2}. \quad (A.14)$$

and the function $h(t,u)$ is

$$h(t,u) = \left[\frac{b_1^2+b_2^2+b_1b_2}{3(b_1-b_2)^2} - \frac{(b_1+b_2)^2}{4(b_1-b_2)^2}\right]u^3 - \frac{1}{4u(b_1-b_2)^2}\left[t^2 + \left(2u^2(b_1+b_2) - 4iau\right)t\right] - \frac{b_1b_2(c_1-c_2)}{b_1-b_2}u + \frac{ia(b_1c_1-b_2c_2)}{b_1-b_2}. \quad (A.15)$$

Next, we integrate over t, and obtain

$$I = \left(\frac{1}{2\pi}\right)^2 \exp\left[-\frac{a(b_1c_1-b_2c_2)}{b_1-b_2}\right] \times \int_{-\infty}^{+\infty} \frac{du}{|b_1-b_2|^3}\sqrt{\frac{i\pi}{\alpha}}\sqrt{\frac{\pi}{i\gamma}}\exp(iq(u)) \quad (A.16)$$

with

$$\gamma = \frac{1}{4u(b_1-b_2)^2} \quad (A.17)$$

and the function $q(u)$

$$q(u) = \left[\frac{b_1^2+b_2^2+b_1b_2}{3(b_1-b_2)^2}\right]u^3 - \frac{ia(b_1+b_2)}{(b_1-b_2)^2}u^2 - \left[\frac{b_1b_2(c_1-c_2)}{b_1-b_2} + \frac{a^2}{(b_1-b_2)^2}\right]u. \quad (A.18)$$

By inserting the expressions for α and γ, the integral I can be simplified to

$$I = \left(\frac{1}{2\pi}\right)\exp\left[-\frac{a(b_1c_1-b_2c_2)}{b_1-b_2}\right]\frac{1}{|b_1-b_2|} \times \int_{-\infty}^{+\infty} du\exp(iq(u)). \quad (A.19)$$

At this point we still need to perform the integral over u. To this end, let us first consider another integral of the following form

$$\tilde{I} = \frac{1}{2\pi}\int_{-\infty}^{+\infty} dx \exp\left[i(Ax^3 - Bx^2 - Cx)\right] \quad (A.20)$$

with $A > 0$. We introduce the variable $x = w+s$ in order to change the integration variable, then

$$\tilde{I} = \frac{1}{2\pi}\exp[is(As^2 - Bs - C)] \int_{-\infty}^{+\infty} dw \exp\left[i(Aw^3 + (3As-B)w^2 + (3As^2 - 2Bs - C)w)\right]. \quad (A.21)$$

To eliminate the quadratic term, we set $s = B/3A$. Thus, this integral can be rewritten as an Airy function

$$\tilde{I} = \frac{1}{(3A)^{1/3}}\exp\left[-\frac{iB}{3A}\left(\frac{2B^2}{9A} + C\right)\right] \times \mathrm{Ai}\left(-\frac{1}{(3A)^{1/3}}(\frac{B^2}{3A} + C)\right). \quad (A.22)$$

Now if we look at the expression of the function $q(u)$ in Eq. (A.18), we find that to evaluate the original integral I , we just need to calculate the integral $\tilde{I}$ in A.20 by taking the parameters

$$3A = \frac{b_1^2+b_2^2+b_1b_2}{(b_1-b_2)^2} = \frac{b_1^3-b_2^3}{(b_1-b_2)^3} \quad (A.23a)$$

$$B = \frac{ia(b_1+b_2)}{(b_1-b_2)^2} \quad (A.23b)$$

$$C = \frac{b_1b_2(c_1-c_2)}{b_1-b_2} + \frac{a^2}{(b_1-b_2)^2}. \quad (A.23c)$$

Using the result from Eq. (A.22), we have

$$\tilde{I} = \frac{b_1 - b_2}{(b_1^3 - b_2^3)^{1/3}} \times \exp\left\{\frac{a^3(b_1^3 + b_2^3)}{3(b_1^3 - b_2^3)^2} + \frac{ab_1b_2(b_1 + b_2)(c_1 - c_2)}{b_1^3 - b_2^3}\right\} \times \mathrm{Ai}\left(\frac{a^2 b_1 b_2}{(b_1^3 - b_2^3)^{4/3}} - \frac{b_1 b_2 (c_1 - c_2)}{(b_1^3 - b_2^3)^{1/3}}\right). \tag{A.24}$$

Finally, we arrive at the result for the original integral

$$I = \frac{e^{\sigma}\mathrm{Ai}(\xi)}{(b_1^3 - b_2^3)^{1/3}} \qquad (b_1 > b_2) \tag{A.25a}$$

$$\sigma = \frac{a^3(b_1^3 + b_2^3)}{3(b_1^3 - b_2^3)^2} - \frac{a(b_1^3 c_1 - b_2^3 c_2)}{b_1^3 - b_2^3} \tag{A.25b}$$

$$\xi = \frac{a^2 b_1 b_2}{(b_1^3 - b_2^3)^{4/3}} - \frac{b_1 b_2 (c_1 - c_2)}{(b_1^3 - b_2^3)^{1/3}}. \tag{A.25c}$$

Although we arrived at an analytical expression for this integral, there is still one problem in getting numerical values from this expression when $b_1 \simeq b_2$, since the denominator goes to zero and the exponential diverges. Hence, we need to get an asymptotic expression for $b_1 \to b_2$. Let

$$b_1^3 = b^3 + \epsilon \tag{A.26a}$$

$$b_2^3 = b^3 - \epsilon \tag{A.26b}$$

where $\epsilon \to 0^+$. Then we have

$$\sigma = \frac{a^3(b_1^3 + b_2^3)}{12\epsilon^2} - \frac{a(b_1^3 c_1 - b_2^3 c_2)}{2\epsilon} \tag{A.27}$$

$$\xi = \frac{a^2 b_1 b_2}{(2\epsilon)^{4/3}}\left(1 - \frac{2(c_1 - c_2)\epsilon}{a^2}\right). \tag{A.28}$$

Since as $\epsilon \to 0$, $\xi \to +\infty$. We can take the asymptotic expression for the Airy function

$$\mathrm{Ai}(\xi) \sim \frac{\exp\left[-\frac{2}{3}\xi^{\frac{3}{2}}\right]}{2\sqrt{\pi}\xi^{1/4}} \tag{A.29}$$

for $\xi \to +\infty$. We obtain

$$\lim_{\epsilon \to 0^+} I(\epsilon) = \frac{1}{2\sqrt{\pi}\xi^{1/4}(2\epsilon)^{1/3}} \exp\left[\sigma - \frac{2}{3}\xi^{\frac{3}{2}}\right]. \tag{A.30}$$

Let us first calculate the term appearing in the exponent. Since

$$b_1^3 + b_2^3 = 2b^3 \tag{A.31}$$

$$(b_1 b_2)^{3/2} = b^3\sqrt{1 - \epsilon^2/b^6} \tag{A.32}$$

$$b_1^3 c_1 - b_2^3 c_2 = b^3(c_1 - c_2) + (c_1 + c_2)\epsilon, \tag{A.33}$$

we have

$$\sigma = \frac{a^3 b^3}{6\epsilon^2} - \frac{ab^3(c_1 - c_2)}{2\epsilon} - \frac{a(c_1 + c_2)}{2} \tag{A.34}$$

and

$$\begin{aligned}\xi^{\frac{3}{2}} &= \frac{a^3(b_1 b_2)^{3/2}}{4\epsilon^2}\left(1 - \frac{2(c_1 - c_2)\epsilon}{a^2}\right)^{3/2} \\ &= \frac{a^3 b^3}{4\epsilon^2}\left[\left(1 - \frac{\epsilon^2}{b^6}\right)\left(1 - \frac{2(c_1 - c_2)\epsilon}{a^2}\right)^3\right]^{1/2} \\ &= \frac{a^3 b^3}{4\epsilon^2}\left[1 - \frac{3(c_1 - c_2)\epsilon}{a^2} + \left(\frac{3(c_1 - c_2)^2}{2a^4} - \frac{1}{2b^6}\right)\epsilon^2\right] \\ &\quad + O(\epsilon).\end{aligned} \tag{A.35}$$

We get

$$\sigma - \frac{2}{3}\xi^{\frac{3}{2}} = -\frac{a(c_1 + c_2)}{2} - \frac{b^3(c_1 - c_2)^2}{4a} + \frac{a^3}{12b^3} + O(\epsilon). \tag{A.36}$$

Next, we calculate the factor in front of the exponent. Since

$$\xi^{1/4} = \frac{\sqrt{a}(b_1 b_2)^{1/4}}{(2\epsilon)^{1/3}}\left(1 - \frac{2(c_1 - c_2)\epsilon}{a^2}\right)^{1/4}, \tag{A.37}$$

we have

$$\begin{aligned}\frac{1}{2\sqrt{\pi}\xi^{1/4}(2\epsilon)^{1/3}} &= \frac{1}{2\sqrt{a\pi b}}\left[\left(1 - \frac{\epsilon^2}{b^6}\right)\left(1 - \frac{2(c_1 - c_2)\epsilon}{a^2}\right)^3\right]^{-\frac{1}{12}} \\ &= \frac{1}{2\sqrt{ab\pi}}\left[1 + \frac{(c_1 - c_2)\epsilon}{2a^2} - \left(\frac{7(c_1 - c_2)^2}{8a^4} - \frac{1}{12b^6}\right)\epsilon^2\right] + O(\epsilon^3).\end{aligned} \tag{A.38}$$

At last, we have

$$I(\epsilon) = \frac{1}{2\sqrt{ab\pi}}\left[1 + \frac{(c_1 - c_2)\epsilon}{2a^2} - \left(\frac{7(c_1 - c_2)^2}{8a^4} - \frac{1}{12b^6}\right)\epsilon^2 + O(\epsilon^3)\right]\exp\left[\frac{a^3}{12b^3} - \frac{a(c_1 + c_2)}{2} - \frac{b^3(c_1 - c_2)^2}{4a} + O(\epsilon)\right] \tag{A.39}$$

and the leading term in the asymptotic limit is

$$\lim_{\epsilon\to 0^+} I(\epsilon) = \frac{1}{2\sqrt{ab\pi}} \exp\left[\frac{a^3b^3}{72} - \frac{a(c_1+c_2)}{2} - \frac{b^3(c_1-c_2)^2}{4a}\right]. \tag{A.40}$$

[1] J. Mikosch et al., Science **319**, 183 (2008).
[2] J. Mikosch et al., J. Am. Chem. Soc. **135**, 4250 (2013).
[3] H. Guo, Int. Rev. Phys. Chem. **31**, 1 (2012).
[4] J. Hirschfelder, H. Eyring, and B. Topley, J. Chem. Phys. **4**, 170 (1936).
[5] H. M. Hulburt and J. O. Hirschfelder, J. Chem. Phys. **11**, 276 (1943).
[6] L. Bonnet, Int. Rev. Phys. Chem **32**, 171 (2013).
[7] G. Nyman and H.-G. Yu, Int. Rev. Phys. Chem **32**, 39 (2013).
[8] W. Hu and G. C. Schatz, J. Chem. Phys. **125**, 132301 (2006).
[9] L. J. Butler, Ann. Rev. Phys. Chem. **49**, 125 (1998).
[10] D. R. Yarkony, J. Phys. Chem. **100**, 18612 (1996).
[11] T.-S. Chu, Y. Zhang, and K.-L. Han, Int. Rev. Phys. Chem. **25**, 201 (2006).
[12] G. J. Halász, A. Vibók, R. Baer, and M. Baer, J. Chem. Phys. **124**, 081106 (2006).
[13] J. C. Tully, J. Chem. Phys. **137**, 22A301 (2012).
[14] L. Sheps et al., Science **328**, 220 (2010).
[15] H. J. Woerner et al., Science **334**, 208 (2011).
[16] E. Garand, J. Zhou, D. E. Manolopoulos, M. H. Alexander, and D. M. Neumark, Science **319**, 72 (2008).
[17] C. Shin and S. Shin, J. Chem. Phys. **113**, 6528 (2000).
[18] M. Baer, Phys. Rep. **358**, 75 (2002).
[19] R. Baer, Chem. Phys. Lett. **364**, 75 (2002).
[20] I. Tavernelli, E. Tapavicza, and U. Rothlisberger, J. Chem. Phys. **130**, 124107 (2009).
[21] I. Tavernelli, B. F. E. Curchod, A. Laktionov, and U. Rothlisberger, J. Chem. Phys. **133**, 194104 (2010).
[22] C. Hu, O. Sugino, and K. Watanabe, J. Chem. Phys. **135**, 074101 (2011).
[23] S. Shin and H. Metiu, J. Chem. Phys. **102**, 9285 (1995).
[24] O. I. Tolstikhin and L. B. Madsen, Phys. Rev. Lett. **111**, 153003 (2013).
[25] A. Abedi, F. Agostini, Y. Suzuki, and E. K. U. Gross, Phys. Rev. Lett. **110**, 263001 (2013).
[26] P. Vindel-Zandbergen, M. Falge, B. Chang, V. Engel, and I. Sola, Theor. Chem. Acc. **132**, 1 (2013).
[27] M. Falge, V. Engel, and S. Gräfe, J. Phys. Chem. Lett. **3**, 2617 (2012).
[28] K. Hader and V. Engel, J. Chem. Phys. **136**, 104306 (2012).
[29] M. Falge, V. Engel, and S. Gräfe, J. Chem. Phys. **134**, 184307 (2011).
[30] K. Hader and V. Engel, Chem. Phys. Lett. **509**, 119 (2011).
[31] A. Kuppermann, J. A. Kaye, and J. P. Dwyer, Chem. Phys. Lett. **74**, 257 (1980).
[32] V. Lopez, V. K. Babamov, and R. A. Marcus, J. Chem. Phys. **81**, 3962 (1984).
[33] V. K. Babamov, V. Lopez, and R. A. Marcus, J. Chem. Phys. **78**, 5621 (1983).
[34] V. K. Babamov, V. Lopez, and R. Marcus, Chem. Phys. Lett. **101**, 507 (1983).
[35] R. Levine, Mol. Phys. **22**, 497 (1971).
[36] V. Aquilanti and S. Cavalli, J. Chem. Soc., Faraday Trans. **93**, 801 (1997).
[37] N. E. Henriksen and F. Y. Hansen, *Theories of Molecular Reaction Dynamics*, Oxford University Press, New York, 2008.
[38] L. E. Fernandez, S. Horvath, and S. Hammes-Schiffer, J. Phy. Chem. Lett. **4**, 542 (2013).
[39] B. Auer, A. V. Soudackov, and S. Hammes-Schiffer, J. Phys. Chem. B **116**, 7695 (2012).
[40] L. E. Fernandez, S. Horvath, and S. Hammes-Schiffer, J. Phys. Chem. C **116**, 3171 (2012).